

Local Time Variation in the Large-Scale Structure of Saturn's Magnetosphere

Key Points:

- We use hot plasma pressure observations to update the UCL/AGA model of Saturn's magnetodisk
- We investigate how local time variations in hot plasma and effective disk radius influence the magnetic field structure
- We find variability in current sheet thickness, density, and ionospheric field line mappings

Supporting Information:

- Supporting Information S1
- Table S2
- Table S3

Correspondence to:

A. M. Sorba,
arianna.sorba.15@ucl.ac.uk

Citation:

Sorba, A. M., Achilleos, N. A., Sergis, N., Guio, P., Arridge, C. S., & Dougherty, M. K. (2019). Local time variation in the large-scale structure of Saturn's magnetosphere. *Journal of Geophysical Research: Space Physics*, 124. <https://doi.org/10.1029/2018JA026363>

Received 6 DEC 2018

Accepted 16 JUL 2019

Accepted article online 29 JUL 2019

A. M. Sorba^{1,2} , N. A. Achilleos^{1,2} , N. Sergis^{3,4} , P. Guio^{1,2} , C. S. Arridge⁵ ,
and M. K. Dougherty⁶ 

¹Department of Physics and Astronomy, University College London, London, UK, ²Centre for Planetary Sciences, UCL/Birkbeck, London, UK, ³Office for Space Research and Technology, Academy of Athens, Athens, Greece, ⁴Institute of Astronomy, Astrophysics, Space Applications, and Remote Sensing, National Observatory of Athens, Athens, Greece, ⁵Department of Physics, Lancaster University, Lancaster, UK, ⁶Space and Atmospheric Physics Group, Blackett Laboratory, Imperial College London, London, UK

Abstract The large-scale structure of Saturn's magnetosphere is determined by internal and external factors, including the rapid planetary rotation rate, significant internal hot and cold plasma sources, and varying solar wind pressure. Under certain conditions the dayside magnetospheric magnetic field changes from a dipolar to more disk-like structure, due to global force balance being approximately maintained during the reconfiguration. However, it is still not fully understood which factors dominantly influence this behavior, and in particular how it varies with local time. We explore this in detail using a 2-D force-balance model of Saturn's magnetodisk to describe the magnetosphere at different local time sectors. For model inputs, we use recent observational results that suggest a significant local time asymmetry in the pressure of the hot (>3 keV) plasma population, and magnetopause location. We make calculations under different solar wind conditions, in order to investigate how these local time asymmetries influence magnetospheric structure for different system sizes. We find significant day/night asymmetries in the model magnetic field, consistent with recent empirical studies based on *Cassini* magnetometer observations. We also find dawn-dusk asymmetries in equatorial current sheet thickness, with the varying hot plasma content and magnetodisk radius having comparable influence on overall structure, depending on external conditions. We also find significant variations in magnetic mapping between the ionosphere and equatorial disk, and ring current intensity, with substantial enhancements in the night and dusk sectors. These results have consequences for interpreting many magnetospheric phenomena that vary with local time, such as reconnection events and auroral observations.

1. Introduction

A magnetosphere is a magnetic and plasma structure that surrounds a magnetized planet, due to the interaction between the planetary magnetic field and the solar wind. At Saturn, the large-scale configuration of the magnetosphere is determined by a number of factors; the rapid (~ 10.7 -hr period) rotation rate of the planet (Desch & Kaiser, 1981) and significant internal plasma population originating from the cryovolcanic moon Enceladus (Dougherty et al., 2006) give rise to a “disk-like” magnetic field structure. In the outer magnetosphere, beyond $\sim 15 R_S$ (where R_S is Saturn's radius, 60,268 km), the magnetospheric magnetic field lines are radially stretched outward in the equatorial plane compared to a dipolar configuration. This is supported by an equatorial azimuthal ring current, such that the associated magnetic pressure and curvature forces balance the centrifugal force acting radially outward on the rapidly rotating plasma. The centrifugal force can be directly linked to an inertial current, which contributes to the total ring current; this inertial component is equivalent to the azimuthal drift associated with centrifugal force in a frame corotating with the plasma. In the middle and outer magnetosphere, beyond $\sim 10 R_S$, there is also a significant population of hotter (>3 keV for ions) and more variable plasma, which also contributes to the formation of a magnetodisk structure, via an enhancement of the ring current (Sergis et al., 2010). This relationship is discussed in more detail in the next section via equation (1). In addition, pressure balance between the magnetosphere and the varying external solar wind pressure conditions typically determines the approximate shape and size of the magnetosphere (Pilkington et al., 2015a). Changes in magnetopause morphology in turn influences the internal magnetic field configuration. Both modeling and observational studies have shown that

the dayside magnetic field changes configuration to become more disk-like when the system expands to a larger size (Achilleos et al., 2010; Arridge et al., 2008; Bunce et al., 2008; Sorba et al., 2017).

The relative importance of each of these factors in controlling Saturn's magnetospheric structure is currently an area of active research. In recent years, a more global understanding of Saturn's magnetosphere has become possible largely thanks to the extensive temporal, spatial, and seasonal coverage of the *Cassini* space mission, which toured the Saturnian magnetosphere from 2004 to 2017. In particular, there is now an opportunity to investigate in more detail how the large-scale structure of Saturn's magnetosphere varies with *local time*, and which factors control this behavior. This information is important for interpreting a range of phenomena at Saturn, for example, the likelihood of reconnection events in different regions of the magnetosphere (Delamere et al., 2015), which is related to how current sheet thickness varies with local time (Kellett et al., 2011). Understanding more about the structure of the current sheet is also important for studies of the observed periodicities at Saturn's magnetosphere, which investigate how the position and thickness of the equatorial current sheet are modulated at a period close to the planetary rotation rate (e.g., Cowley & Provan, 2017; Thomsen et al., 2017). More generally, a good picture of the global magnetic field structure at different local times is important for understanding how different regions of the magnetosphere magnetically map to the polar ionosphere in different local time sectors, for example, when interpreting observations of Saturn's aurora.

A recent empirical study of magnetopause crossings by Pilkington et al. (2015b) showed evidence of a dawn-dusk asymmetry in the location of the magnetopause boundary, while a survey of magnetospheric plasma populations from Sergis et al. (2017) showed significant local time asymmetry in the hot plasma population, with enhanced pressures in the dusk and midnight local time sectors compared to dawn and noon. These factors will influence the magnetic and plasma configuration of the magnetosphere differently at different local times. In addition, a recent magnetic field model by Carbary (2018) shows significant day-night asymmetry in equatorial-ionospheric magnetic mapping profiles, and local time asymmetries in the location of Saturn's aurora have been observed in studies such as Badman et al., (2006, 2011).

In this work we investigate the relative importance of these factors in controlling magnetospheric structure at different local time sectors using a modeling approach, to complement observational studies. We use the University College London/Achilleos-Guio-Arridge (UCL/AGA) model, a 2-D force-balance magnetic and plasma model of Saturn's magnetodisk from Achilleos et al. (2010). We adapt this model to describe the typical, equilibrium conditions of Saturn's magnetosphere at four different local time sectors; noon (09:00–15:00), dawn (03:00–09:00), dusk (15:00–21:00), and night (21:00–03:00). We use equatorial profiles of the hot plasma pressure from Sergis et al. (2017) for the different local time sectors as boundary condition inputs to the magnetodisk model and determine appropriate magnetopause radius values to use for each sector based on the magnetopause surface model of Pilkington et al. (2015b). Our method of constructing these models is described in section 2. In section 3 we present the results of these calculations and highlight interesting comparisons in the magnetic field structure, azimuthal current density, and magnetic mappings for the different local time sectors. Section 4 provides a brief summary of the main conclusions of this work.

2. Method

2.1. The UCL/AGA Force-Balance Magnetodisk Model

In this study we used a modified version of the UCL/AGA magnetic field and plasma model first described by Achilleos et al. (2010), itself based on a model originally constructed for the Jovian magnetodisk by Caudal (1986), adapted for Saturn. More information can be found in those studies. The model is axisymmetric about the planetary dipole/rotation axis, which are assumed to be parallel. This parallel assumption is appropriate for Saturn in particular, as the rotation and dipole axes are aligned to within 0.01° (Dougherty et al., 2018). This axisymmetric assumption is appropriate as an approximation of the large-scale structure of the magnetic field, as shown by Hunt et al. (2014), who compared the gradients of currents in radial, azimuthal, and meridional directions and found the azimuthal gradients could be neglected. The model is constructed based on the assumption of force balance in the rotating plasma of the magnetosphere between the Lorentz body force (magnetic pressure and tension forces), pressure gradient force, and centrifugal force, such that

$$\mathbf{J} \times \mathbf{B} = \nabla P - nm_i \omega^2 \rho \hat{\rho}, \quad (1)$$

where J is the current density, B is the magnetic field vector, and ρ is cylindrical radial distance from the rotation/dipole axis, with $\hat{\rho}$ its unit vector. The plasma properties are isotropic pressure P , ion number density n , mean ion mass m_i , and angular velocity ω . Equatorial radial profiles of these plasma properties are required boundary conditions for this model and were obtained from studies based on observations from the Cassini plasma instruments CAPS (CASSINI Plasma Spectrometer; Young et al., 2004) and MIMI (Magnetospheric IMaging Instrument; Krimigis et al., 2004). These are presented in Achilleos et al. (2010) and updated for this study as described in the following sections. The equatorial radial profile of angular velocity ω necessary to calculate the centrifugal force term was obtained using a recent study of CAPS observations from Wilson et al. (2017), as described in Sorba et al. (2018). The plasma is assumed to consist of a cold population with pressure P_C , confined toward the equatorial plane due to the centrifugal force exerted on it, and a hot population with associated pressure P_H distributed uniformly along magnetic field lines.

Any magnetic field can be represented in terms of two Euler potentials α and β , $B = \nabla\alpha \times \nabla\beta$, as a consequence of magnetic fields being divergence free (Stern, 1970). For an axisymmetric field with no azimuthal component, the forms of α and β can be chosen such that all information about the poloidal field is contained in one Euler potential, which we call α , which is constant along magnetic field lines. Caudal (1986) showed that equation (1) corresponds to a partial differential equation, which can be solved iteratively for α , providing magnetic field and plasma distributions as a function of cylindrical radial distance ρ , and height with respect to the rotational equator z . We say that the model has achieved convergence when the relative difference in α between two successive iterations falls below 0.5%, when using the mean of the current and previous solutions at each iteration (see detailed discussion about this numerical relaxation in Sorba et al., 2018).

This model was originally used to represent typical dayside conditions at Saturn, and so we made various modifications described herein, which are necessary to appropriately represent different local time sectors.

2.2. Hot Plasma Parameterization for Different Local Time Sectors

An important boundary condition for this model is the equatorial profile of hot plasma pressure. It was shown by Achilleos et al. (2010) that variations in this quantity estimated using the spread of observations from, for example, Sergis et al. (2007) can have a significant impact on the magnetic field configuration of a typical dayside model. In Achilleos et al. (2010), the authors used quartile fits to equatorial hot (>3 keV) plasma pressure observations from Cassini MIMI to show that a globally elevated hot plasma pressure and associated pressure gradient causes a more disk-like magnetic field structure, with more radially stretched field lines, due to the enhancement of the equatorial ring current. Achilleos et al. (2010) also found that variations in the hot plasma content affected magnetic mapping between the equatorial disk and the ionosphere. As discussed in section 1, the magnetospheric hot plasma population also affects the compressibility of the magnetopause and overall force balance (Sorba et al., 2017).

More recently, a comprehensive study using Cassini MIMI data (Sergis et al., 2017) showed that the pressure of this hot plasma population not only varies over time and distance but also varies significantly with local time, even when averaged over a large portion of the Cassini mission (July 2004 to December 2013). Sergis et al. (2017) also found that especially in the middle and outer magnetosphere beyond $\sim 11 R_S$ pressure gradients associated with both hot and cold populations contributed more to the total ring current than centrifugal acceleration, except in the noon sector where both contributed approximately equally. Therefore, in this study, we used average equatorial profiles of hot plasma pressure between 5 and $16 R_S$ presented in Sergis et al. (2017) for the different local time sectors, as boundary conditions for our models. Specifically, we fit the $1 R_S$ -width-binned data presented in Sergis et al. (2017) using polynomial functions of the form

$$\log(P_H) = a_0 + a_1\rho + a_2\rho^2 + a_3\rho^3 + a_4\rho^4, \quad (2)$$

following the approach used in Sergis et al. (2017), with each point weighted by the inverse square of the provided standard error of the mean. The resulting coefficients for each sector are shown in Table 1, with pressure in units of nPa and radial distance in units of R_S . The polynomials are shown in Figure 1, as well as the corresponding observations from Sergis et al. (2017), with standard error of the mean of each bin shown by the error bars. This figure shows that the hot plasma pressure is significantly higher in the dusk and night sectors than the dawn and noon sectors. Here the dawn, noon, dusk, and night sectors are defined by the magnetic local time intervals 03:00–09:00, 09:00–15:00, 15:00–21:00, and 21:00–03:00, respectively.

Table 1
Coefficients of Fourth-Order Polynomial Fits to the Logarithm of Each of the Hot Pressure Profiles Shown in Figure 1, as Described in the Main Text

Coefficient	Noon	Dawn	Dusk	Night
a_0	-5.47	-1.96	-1.36	-6.86
a_1	1.10	-0.149	-0.311	2.07
a_2	-0.114	0.0686	0.109	-0.258
a_3	0.00514	-0.00652	-0.0104	0.0137
a_4	-8.47×10^{-5}	1.83×10^{-4}	2.99×10^{-4}	-2.71×10^{-4}

For values of ρ smaller than the applicable range of the polynomials ($5.5 R_S$) we assumed the hot plasma pressure falls linearly to zero with ρ , broadly in line with observations and with the approach of Achilleos et al. (2010). For the dawn profile we used an inner boundary of $6.5 R_S$ due to lack of data in the innermost bin in the Sergis et al. (2017) data, which can be seen in Figure 1. For values of ρ above the applicable range of the polynomials ($15.5 R_S$), we assumed a profile where the product of the hot plasma pressure and the local flux tube volume is constant with radial distance, following previous studies such as Achilleos et al. (2010, 2017). In practice for the dawn and dusk models we used outer limits of 15.3 and $15.1 R_S$, respectively, which are the locations of the local minima in the hot pressure polynomials, to ensure a smoother profile.

2.3. Magnetopause Radius for Different Local Time Sectors

The UCL/AGA magnetodisk model used in this work can also be parameterized by an effective disk radius R_D , the equatorial radial distance of the last closed field line in the model. As discussed in section 1, variations in this quantity also significantly impact the resulting magnetic field structure in the model, with more expanded systems (larger R_D) having a more disk-like magnetic field structure, that is, more radially “stretched” field lines (e.g., Achilleos et al., 2010; Sorba et al., 2017). This relationship is due to overall force balance in the magnetosphere requiring a larger magnetic tension force with a smaller radius of curvature for more expanded systems. This is also seen in observational studies such as Arridge et al. (2008), who find that in the noon sector, Saturn’s magnetosphere only shows a significant divergence from a dipolar field structure for a magnetopause radius greater than $\sim 23 R_S$. They also find that in contrast, the magnetodisk structure is consistently observed on the flanks and nightside, where the magnetopause radius is greater.

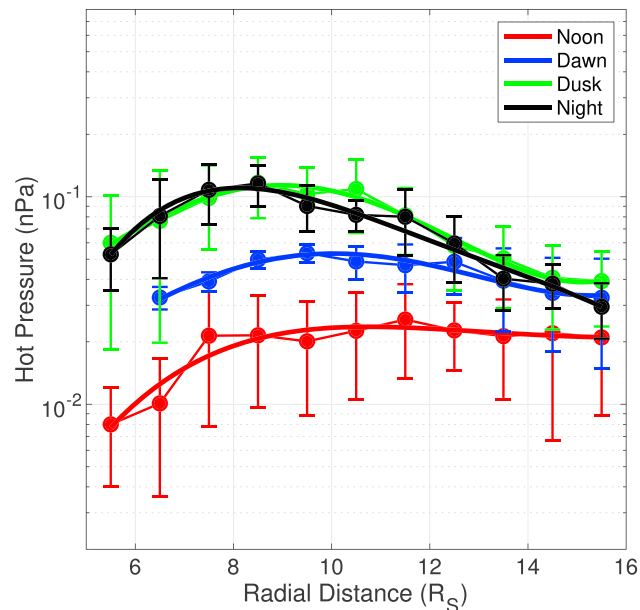


Figure 1. Equatorial radial profiles of hot plasma pressure for different local time sectors, as shown by the color. Solid circles and error bars are means and standard errors for binned data from Sergis et al. (2017), and solid lines are fourth-order polynomial fits to the logarithms of the data points, as described in the main text.

Table 2
Configuration Details for the Two Families of Models Used to Represent Different local Time Sectors, for Compressed (High Solar Wind Dynamic Pressure) and Expanded (Low Solar Wind Dynamic Pressure) Regimes

Regime	LT sector	Disk radius (R_S)	Shield B_z (nT)	D_p estimate (nPa)
Compressed	Noon	21.0	-2.62	0.032
	Dawn	34.3	-0.97	0.026
	Dusk	33.2	-0.88	0.030
	Night	42.0	0.14	—
Expanded	Noon	27.0	-1.40	0.012
	Dawn	43.8	-0.47	0.015
	Dusk	42.3	-0.41	0.016
	Night	54.0	0.13	—

Note. Magnetodisk radius, shielding magnetic field value, and an estimate for the solar wind dynamic pressure D_p are shown for each model.

It was therefore important for this work that we chose appropriate values of the disk radius R_D for each of the local time sectors we were describing. To do this, we appealed to the study of Pilkington et al. (2015b), who improved the earlier Saturn magnetopause surface models of Arridge et al. (2006, 2015a, 2010) by in particular including a small dawn-dusk asymmetry in magnetopause radius in the model. In Pilkington et al. (2015b), the authors used observations of magnetopause crossings made throughout a large portion of the Cassini mission to constrain parameters for a Shue et al. (1997)-type magnetopause model, introducing an extra parameter to describe the dawn-dusk asymmetry. They found that on average the magnetopause boundary extends farther from the planet on the dawnside than the duskside, by $\sim 7\%$. The authors suggested this may be due to a combination of factors including asymmetries in internal pressure populations, and intrinsic asymmetry in plasma flow around the planet with respect to the direction of solar wind flow, with the flows in approximately opposite directions at dawn pushing the magnetopause further out in this sector.

In order to investigate how local time variation in magnetospheric structure varies with system size, we calculated two sets of models under different solar wind dynamic pressure conditions; a compressed regime with subsolar magnetopause radius fixed at $21 R_S$ and an expanded regime with subsolar magnetopause radius fixed at $27 R_S$, following the bimodal values observed in Pilkington et al. (2015a) and Achilleos et al. (2008). For the corresponding dawn and dusk disk radii, we calculated the magnetopause radius at the center of each local time sector (06:00 for dawn and 18:00 for dusk) using the best fit parameters given in Pilkington et al. (2015a, 2015b). We used a value of the nose plasma $\beta = 3$ (where β is the ratio of plasma pressure to magnetic pressure), which is the median value for the data set quoted in Pilkington et al. (2015a), although for a fixed subsolar radius this choice of β had very little impact on the resulting flank radii. Thus, we determined the appropriate disk radii R_D for noon, dawn, and dusk local time sectors, for both high and low solar wind pressure conditions. The resulting values are shown in Table 2. In the absence of an accurate magnetopause model for the nightside of Saturn's magnetosphere, we used a disk radius of twice the subsolar magnetopause radius to represent an approximate nightside local time sector structure.

The solar wind dynamic pressure corresponding to a given equilibrium magnetodisk model can be estimated by assuming pressure balance across the boundary at the equator, as in Sorba et al. (2017). Specifically, we can assume

$$\frac{B_{MS}^2}{2\mu_0} + P_{MS} = \left[k \cos^2(\psi) + \frac{k_B T_{SW}}{1.16 m_p u_{SW}^2} \sin^2(\psi) \right] D_p, \quad (3)$$

where terms on the left-hand side represent the magnetospheric (hence MS subscript) magnetic and plasma pressures just inside the magnetopause boundary and the terms on the right (the coefficients of upstream solar wind dynamic pressure D_p) represent the component of solar wind dynamic pressure incident on the magnetopause surface, and a smaller component associated with the solar wind's thermal pressure. $k = 0.881$ is a factor to account for the diversion of flow around the magnetosphere obstacle (see Spreiter et al., 1966), T_{SW} and u_{SW} are the temperature and speed of the solar wind, and ψ is the angle between

the incident solar wind and the magnetopause surface normal. This same relationship was also used in Pilkington et al. (2015a) to estimate solar wind dynamic pressure based on internal magnetospheric observations and was initially proposed in this form by Kanani et al. (2010), based on the original formulation by Petrinec and Russell (1997).

We used values for B_{MS} and $P_{MS} = P_H + P_C$ extracted just inside the magnetopause boundary of each model and obtained ψ from the Pilkington et al. (2015a) magnetopause surface model at the appropriate local time sector. Finally, we assumed typical parameters $k_B T_{SW} = 100$ eV and $u_{SW} = 460$ km/s following Pilkington et al. (2015a). The resulting estimates of D_P are shown in Table 2. This approach is not appropriate for the far nightside tail, where a concept of ψ is not directly applicable, and so we do not attempt to estimate D_P for those sector models. While the values of D_P do not exactly agree for all compressed or all expanded models, we can see that the two regimes provide significantly different, self-consistent estimates; the mean D_P estimates are 0.029 ± 0.003 nPa and 0.014 ± 0.002 nPa for the compressed and expanded regimes, respectively. Therefore our two families of models, compressed and expanded, broadly correspond to systems under different solar wind conditions, while representing typical internal conditions.

It is also interesting to note that there is evidence that Saturn's magnetopause boundary position is periodically modulated at a rate close to planetary rotation rate, independent of changes in incident solar wind dynamic pressure. This was first suggested by Espinosa and Dougherty (2001) and Espinosa et al. (2003) based on observations from *Pioneer 11* magnetic field data. Later, Clarke et al. (2010) analyzed Cassini magnetometer (MAG; Dougherty et al., 2004) and CAPS electron spectrometer data and found that Saturn's dayside magnetopause was periodically displaced by up to $5 R_S$ in the postnoon local time sector, associated with rotating perturbations in internal magnetic field and plasma properties. Magnetohydrodynamic (MHD) simulations of Saturn's magnetosphere presented in Kivelson and Jia (2014) showed similar behavior, with constant solar wind properties in their models such that the observed perturbations were again driven by periodic perturbations in internal processes. Kivelson and Jia (2014) and later Ramer et al. (2017) explored how this modulation in magnetopause position may vary across local time sectors and found a complicated relationship between the phase of the rotating perturbation and its effect on the magnetosphere morphology depending on the local time.

Varying the magnetopause radius in such a way would affect the magnetic field and plasma properties predicted by our magnetodisk models for a given local time sector, similarly to how our model predictions vary for compressed and expanded regimes (as discussed later in this study). In Sorba et al. (2018), the authors used forms of the UCL/AGA magnetodisk model to try and characterize these periodic perturbations in Cassini magnetic field data in the outer magnetosphere around the dusk sector. They used a family of magnetodisk models calculated at different magnetopause radii and organized with planetary longitude (but not local time) to represent a rotational perturbation in current sheet thickness, with a thicker current sheet represented by a model with a smaller magnetodisk radius. As in this study, Sorba et al. (2018) calculated that the estimated effective solar wind dynamic pressure associated with each magnetodisk model was different and so the family of models did not represent a system under constant solar wind dynamic pressure. However, Sorba et al. (2018) found that their approach could still characterize the phase and amplitude of the perturbations particularly in the meridional component of the magnetic field data. A deepened understanding of how the large-scale structure of Saturn's magnetosphere varies across local time would further help with future studies of this nature.

2.4. Magnetodisk Model Adaptations

Finally, we made minor adaptations to the magnetodisk model construction in order to be more appropriate for different local time sectors. In Achilleos et al. (2010) the authors include a small, uniform, southward-directed "shielding field" to the total magnetic field at every iteration, to approximately account for the magnetic field associated with the magnetopause and magnetotail current sheets. The magnitude of this field was chosen by calculating dayside equatorial averages of the empirical field models of Alexeev and Belenkaya (2005) and Alexeev et al. (2006), and it varied with model magnetodisk radius R_D (see Achilleos et al., 2010, Figure 6). For this study, we calculated local time sector averages of these field models over circular segments with radius R_D , to account for the increased significance of the tail current field compared to the magnetopause current field for nightside local time sectors in particular. We also enhanced the field associated with the magnetopause current beyond a dipole approximation by a factor $(1 + k_{MD})$, where k_{MD} is the ratio of the ring current and planetary dipole magnetic moments, as in Sorba et al. (2018),

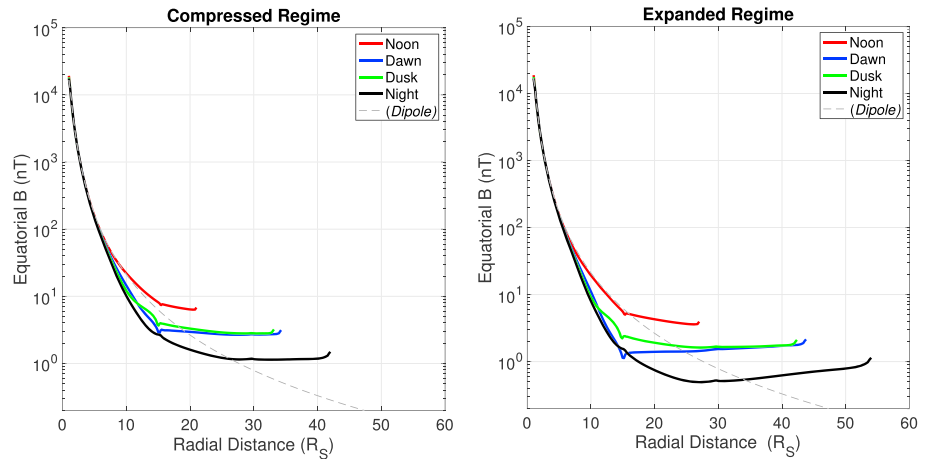


Figure 2. Equatorial profiles of total magnetic field strength B with radial distance for each local time sector as shown by the color, for both the compressed (a) and expanded (b) regimes. On each plot a profile for a dipole magnetic field is shown in dashed gray for comparison.

following Alexeev and Belenkaya (2005). As in Sorba et al. (2018), to estimate the appropriate k_{MD} for each model, we employed an extrapolation of the empirical linear fit from Bunce et al. (2007), although here we used our values of R_D rather than the subsolar magnetopause radius to estimate k_{MD} as we found that this in particular improved convergence in our models. The resulting values for the shielding magnetic field B_z for each model are shown in Table 2. It can be seen that, as expected, the total shielding field decreases and becomes northward directed for the nightside models due to the increased influence of the more northward field associated with the distant tail currents, compared to the more southward field associated with magnetopause currents. While the use of these shielding field values does not significantly affect the global magnetic field structure of the resulting models, we find it does improve the ability for our models to achieve convergence as defined above, compared to model calculations using the same system size and hot plasma content parameters but the approach of Sorba et al. (2018).

We also updated the representation of the cold equatorial ion temperatures used as a boundary condition in the magnetodisk model, using a recent comprehensive survey of equatorial Cassini CAPS observations from Wilson et al. (2017). We fit the equatorial profiles of parallel and perpendicular temperatures for hydrogen and water group ions between 5.5 and $30 R_S$ presented in Wilson et al. (2017) with fourth-order polynomials, with points weighted by the inverse square of the error (assumed to be half the interquartile range of each bin). We then derived a single equatorial plasma temperature profile for the magnetodisk model as in Achilleos et al. (2010), who used the same approach but with earlier more restricted data sets from Wilson et al. (2008) and McAndrews et al. (2009). The best fit polynomials for each ion species and temperature moment are given in the supporting information. We found that this update using a much more comprehensive data set did not significantly affect the overall resulting magnetic field profile of the magnetodisk model, in general causing only a slight increase in magnetic field strength in the inner magnetosphere and slight decrease in the outer magnetosphere, with a maximum difference under 1 nT. However, this update did improve model estimates of the cold plasma pressure, reducing the values in the outer magnetosphere such that they showed better agreement with recent observations from Sergis et al. (2017; also based on CAPS data). This modification is an improvement resulting from better radial coverage and global constraint of the cold plasma temperature than in previous studies.

3. Results and Discussion

3.1. Magnetic Field Structure

The equatorial magnetic field profiles from the resulting magnetodisk models for each local time sector are shown in Figure 2. For comparison, a representative profile for the internal planetary dipole magnetic field is shown by the gray dashed line on each plot.

For the dayside (noon) models, we can see that the magnetic field is approximately dipolar in the inner ($\lesssim 10 R_S$) magnetosphere and falls more slowly with radial distance than a dipole in the middle

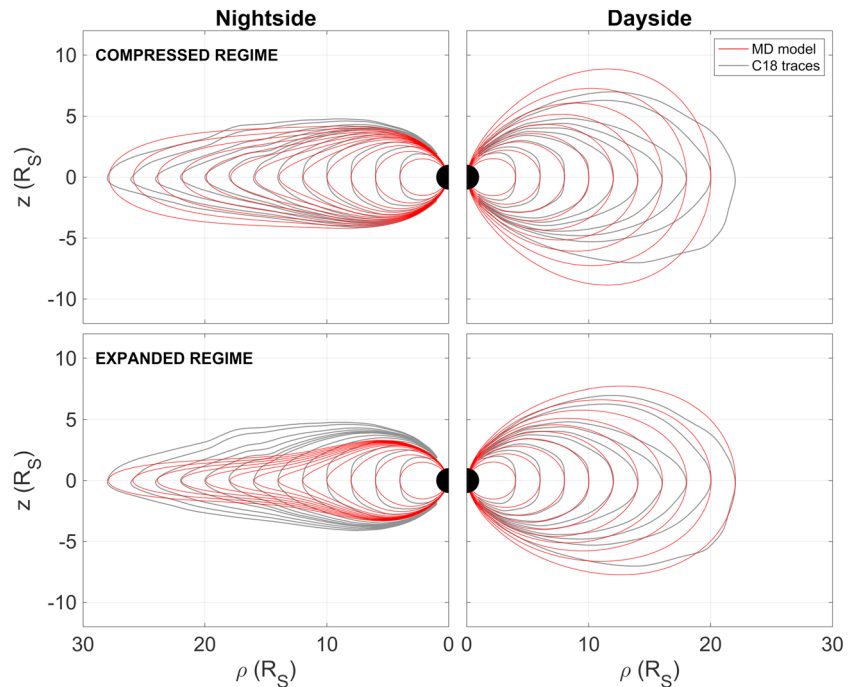


Figure 3. A comparison of model magnetic field lines from Carbery (2018) and this study. In gray are shown traces based on binned Cassini magnetometer meridional magnetic field observations from Carbery, (2018; top and bottom panels an exact reproduction). In red are shown magnetic field lines from the noon and nightside models presented in this study, for the compressed (top panel) and expanded (bottom panel) regimes, for L shells to match those of the Carbery (2018) study.

($10 \lesssim \rho \lesssim 15 R_S$) and outer magnetosphere. This behavior broadly corresponds to a more disk-like magnetic field structure compared to a dipole and appears for a more significant range in radial distance for the expanded noon model. Similar behavior has been found in observational studies of Saturn's magnetosphere. For example, Arridge et al. (2008) showed that the dayside magnetospheric magnetic field was approximately dipolar when the system was compressed, but more disk-like when expanded, particularly beyond a subsolar magnetopause radius of $\sim 23 R_S$. Results of ring current modeling from Bunce et al. (2008) found a similar result. This behavior is expected as a consequence of conservation of magnetic flux threading the equatorial plane of the magnetosphere, such that compressing the system necessarily increases the total magnetic field strength inside the magnetosphere as field lines are pushed together, corresponding to a more dipolar configuration.

For the larger dawn, dusk, and night sector models, the model magnetic field strengths are lower than the corresponding dipole field in the inner magnetosphere and greater in the outer magnetosphere. This too is in line with in situ observations of Saturn's magnetosphere, such as Delamere et al. (2015), who analyzed equatorial current sheet crossings using Cassini MAG data in order to demonstrate how the equatorial magnetic field varies with radial distance in different local time sectors. There is also a small dawn-dusk asymmetry in the magnetic field strengths in our model, with the dusk sector profile persistently higher than the dawn. This is likely due to the asymmetry in magnetopause radius across the sectors, with a larger magnetic field strength at dusk associated with the more compressed system there. This may also be partially associated with the higher hot plasma pressure and associated gradient in the dusk sector requiring a greater magnetic curvature force to balance it. This is interesting to note, as such a small asymmetry in field strength would be unlikely to reveal itself in observational studies of Saturn's magnetosphere, especially due to the relatively poor sampling of the dawn sector equatorial magnetosphere by the Cassini spacecraft over its mission. Previous studies using the UCL/AGA model have not investigated local time variations specifically; however, it was shown in Achilleos et al. (2010, 2014) and Sorba et al. (2018) that this type of model can characterize well the magnetic field measured by Cassini along some individual trajectories, especially when the periodic perturbations in the current sheet are accounted for.

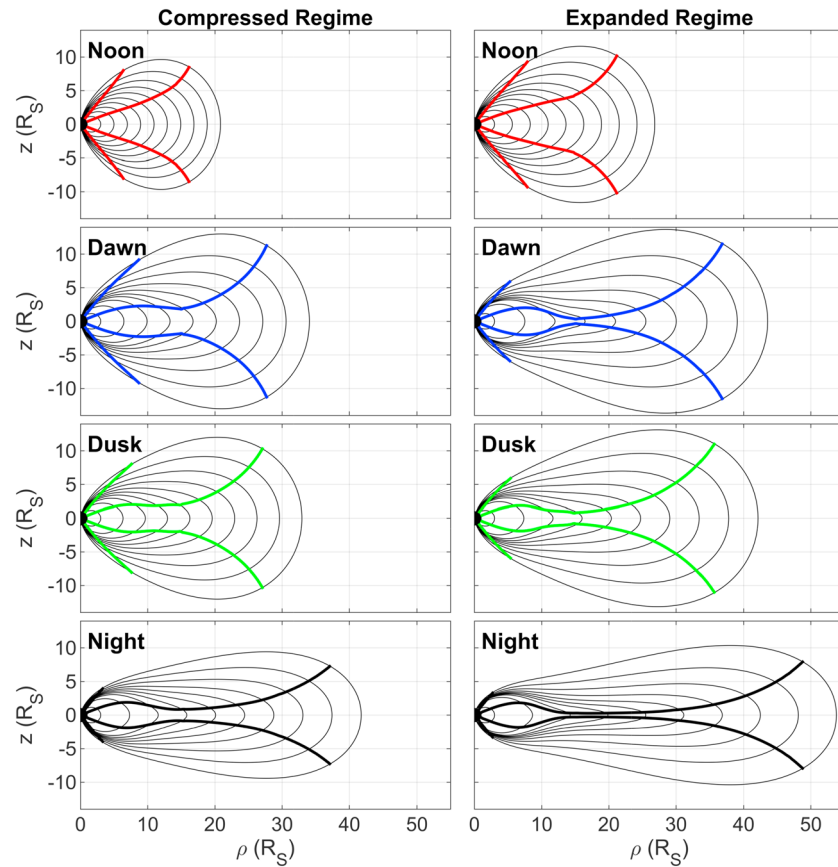


Figure 4. The magnetic field structure for each magnetodisk model for the compressed (left column) and expanded (right column) regimes, shown by the solid black lines. Superposed in color for each model are pairs of lines in each hemisphere, which bound regions where the local magnetic field direction lies within 30° of the $\hat{\rho}$ vector direction.

Looking at the day-night asymmetry in more detail, in Figure 3 we show the magnetic field structure for our noonside and nightside magnetodisk models, for the compressed (top panel) and expanded (bottom panel) regimes in the range $\rho = 4 - 22R_S$ for the dayside and $\rho = 4 - 28R_S$ on the nightside, noting that our compressed dayside model only extends out to $\rho = 21R_S$. For comparison, we include in gray field line traces based on empirical observations from a recent study by Carbary (2018). In that study the author binned magnetic field observations from almost the entire Cassini mission (2004–2016) into two local time sectors, dayside and nightside, and calculated traces using a Runge-Kutta propagator (see Carbary, 2018, and references therein for more details). Carbary (2018) accounted for seasonal warping of the current sheet via a coordinate transformation; however, their model did not account for a change in external solar wind conditions, and so we have reproduced the same traces from Carbary (2018) in the top and bottom panels. We can see that the overall magnetic field structures in our models are similar to those of the Carbary (2018) model, in particular the expanded $27 R_S$ dayside model, and the compressed $42 R_S$ nightside model. Our expanded nightside model shows a magnetic field structure that is significantly more disk-like than the Carbary (2018) analytical model, suggesting that perhaps a magnetodisk radius of $54 R_S$ is somewhat too extreme to accurately characterize the typical midnight magnetosphere. In addition, our compressed dayside model has a significantly more dipolar structure than the Carbary (2018) model results. We should note that here we are comparing specifically our noon (LT 09:00–15:00) and night (LT 21:00–03:00) sector models with the Carbary (2018) traces, which correspond to wider, 12-hr local time regions. Therefore, to more accurately represent, for example, the entire dayside for a more direct comparison, we would need to consider some combination of our noon, dawn, and dusk sector model outputs. This makes it difficult to assess which approach gives a better overall representation of the true Saturn magnetosphere system. However, it can be seen that both our models and the Carbary (2018) results show a transition from a more dipolar magnetic

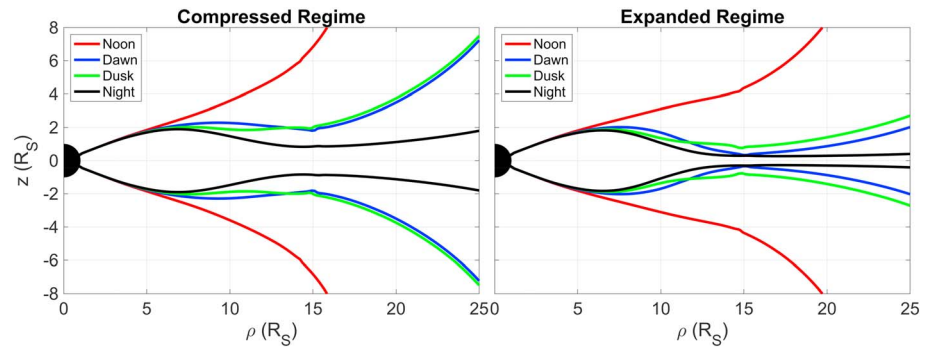


Figure 5. Reproduction of the more equatorward colored lines from Figure 4, for each local time sector model, for compressed (left) and expanded (right) regimes. These represent the low-latitude boundaries of regions where the local magnetic field direction lies within 30° of the $\hat{\rho}$ vector direction.

field configuration when compressed on the dayside to a more stretched, disk-like configuration on the nightside.

In order to investigate more just how disk-like the magnetic field is in each local time sector, we use a visualization technique employed in Bunce et al. (2008), itself based on the analytical approach in Arridge et al. (2008). For each model we bound regions of the magnetosphere where the local magnetic field direction lies within 30° of the $\hat{\rho}$ vector direction such that the field lines are approximately parallel to the equatorial plane. The results are shown in Figure 4, and the reproduction of the most lower latitude of the bounding lines is shown in Figure 5. The magnetic field structure for each model is also shown in black, to further illustrate how this method characterizes the “disky-ness” of the magnetic field structures. These figures show that, as expected, the larger magnetodisk models have significantly more disk-like magnetic field structures in the middle magnetosphere, than the smaller, more dipolar models. As discussed in section 1, this was observed in previous studies such as Arridge et al. (2008), Achilleos et al. (2010), and Sorba et al. (2017) and is a result of how the overall force balance within the magnetosphere changes with system size, in terms of the dominant magnetic and plasma related forces.

In addition, from Figure 5 in particular, it can be seen that, for the compressed regime, the dusk sector has a slightly thinner and more disk-like magnetodisk structure in the middle magnetosphere than the dawn sector, as shown by the bounding lines being more equatorward for the dusk model (shown in green). This effect is likely due to the local enhancement of the ring current in the dusk sector due to the increased hot plasma pressure, which causes a more extreme perturbation from a dipolar magnetic field. This was also discussed in section 1 and observed in Achilleos et al. (2010) and Sorba et al. (2017). Note that this “thinning” of the disk is not the same as thinning of the *plasma* sheet, which is made up of both hot and cold plasma populations. While the *current* sheet and associated *cold* plasma sheet thin, the hot plasma is actually more populous for the thinner, dusk model, and the associated hot plasma pressure is constant along magnetic field lines. The pressure distribution is also affected by particle temperature, or more generally velocity distribution of particles. As described in Sergis et al. (2011) and Arridge et al. (2009), the current sheet, a predominantly magnetic structure, has been observed to be thinner than the plasma sheet it is embedded in, and the plasma sheet itself can have different thicknesses in different particle energies and species.

For the expanded regime, it can be seen in Figure 5 that the opposite relationship is true; in the middle and outer magnetosphere, the dawn sector magnetic field has a thinner and more disk-like structure (shown in blue) than the dusk sector magnetic field (shown in green). This is likely associated with the increased influence of the dawn-dusk asymmetry in effective magnetodisk radius for the expanded regime, as a larger magnetopause radius also promotes a more disk-like structure. For the expanded regime, the dawn magnetopause is $1.5 R_S$ greater than the dusk, compared to $1.1 R_S$ for the compressed regime. It is interesting that this transition in dominant behavior occurs across this compressed-expanded regime threshold. These results suggest that the asymmetries in magnetopause radius and hot plasma content have comparable influence on the global magnetic field structure in those local time sectors. In addition, the expanded system models may be more strongly influenced by the assumption we made that the product of flux tube volume and hot plasma pressure is constant beyond $15.5 R_S$, as described in section 2.2, as this region is by definition

more extended for the expanded system models, where R_D is greater. We hope to relax this assumption with an updated parameterization of the hot plasma pressure beyond $15.5 R_S$ in a future study.

In order to more fully understand the significance of these observed differences between the dawn and dusk configurations, it would be helpful to estimate uncertainties on the positions of these bounding lines. This could involve calculating an ensemble of models with slightly varying input boundary conditions, or perhaps calculating models to varying numbers of iterations, and comparing the outputs. While beyond the scope of this study, this could be pursued in future.

In the aforementioned study by Delamere et al. (2015), the authors find significantly more incidences of “critically thin” equatorial current sheet encounters in the dusk sector than the dawn sector, even when accounting for the sampling bias of Cassini (which spent more time in the dusk sector). This is therefore perhaps more in line with our picture of the compressed regime, with a thinner current sheet on the dusk side due to the influence of the increased hot plasma pressure. However, in general, Delamere et al. (2015) observe that the current sheet is only uniformly thin in the 0:00–6:00 “predawn” local time sector and that in all other sectors the observed meridional magnetic field strength at the current sheet center shows significant variability, with perhaps stronger average magnetic field strengths observed in the postnoon local time sector. In a study from Jia and Kivelson (2016), based on MHD simulations of Saturn’s magnetosphere from Jia et al. (2012), they find a significantly thinner current sheet and more radially stretched magnetic field lines in the dawn sector, which is also observed at Jupiter (e.g., Khurana et al., 2004). This may be understood, as that the simulations of Jia et al. (2012) do not include a suprathermal plasma population, and so the effect of the enhanced hot plasma population on the dusk side is not captured in their study. In addition, it was suggested by Pilkington et al. (2015b) that this absence of suprathermal plasma in the Jia et al. (2012) models may cause their models to slightly overestimate the dawn-dusk asymmetry in magnetopause radius, which predict a mean asymmetry of $2.6 R_S$, compared to $1.5 R_S$ for the Pilkington et al. (2015b) empirical model. Therefore, the results of Jia and Kivelson (2016) may be more strongly influenced by this asymmetry in magnetopause radius, which, as discussed, provides a thinner and more disk-like current sheet in the dawn sector. However, their MHD models do account for plasma acceleration, and azimuthal asymmetry in the magnetic field, which the force-balance models presented in this study do not. Therefore, some dawn-dusk asymmetry in these factors may also influence current sheet thickness in ways that our model cannot capture.

3.2. Ionospheric Field Line Mapping and Azimuthal Current Density

As previously mentioned, varying hot plasma content and magnetopause radius can both affect the mapping of magnetic field lines from the equator to the ionosphere, due to a reconfiguration of the magnetospheric magnetic field structure. It is therefore important to consider how this ionospheric mapping varies for different local time sectors.

The inner boundary of our magnetodisk model is located at a radial locus of $1 R_S$ where $R_S = 60,268$ km, specifically the *equatorial* radius of Saturn at 1-bar atmosphere level. This is greater than the *polar* radius at 1 bar, as Saturn is oblate. Our model therefore does not directly calculate the magnetic field in the polar ionospheric regions, as these regions are closer to the planet than the inner boundary of our model. Also, our model assumes a centered dipole planetary magnetic field. Therefore, we need to account for the oblate spheroid shape of the planet, the altitude of the ionosphere, and effective offset of the planetary dipole in our ionospheric mapping calculations. We do this by calculating the magnetic potential α (see discussion in section 2.1) for a dipole magnetic field with origin offset northward by $z_{\text{off}} = 0.0466 R_S$ (Dougherty et al., 2018), along a surface 1,100-km altitude above an oblate spheroid with equatorial radius 60,268 km and polar radius 54,364 km (Seidelmann et al., 2007). The ionospheric altitude of 1,100 km was chosen following studies from Gérard et al. (2009), Stallard et al. (2012), and others. As the Euler magnetic potential α is constant along a given magnetic field line by definition, we can then map equatorial values of α to values calculated on the oblate ionospheric surface in order to estimate the realistic colatitude at which the magnetic field lines would pierce the northern and southern polar ionospheres.

This approach of mapping equatorial and ionospheric values of α means we are not explicitly following a magnetic field line out into high latitudes but are equating flux functions at the equator and the ionosphere regions where the magnetic field models are well constrained. This mitigates our sensitivity to the high-latitude loci of the field lines predicted by our models. In addition, similar mappings of UCL/AGA

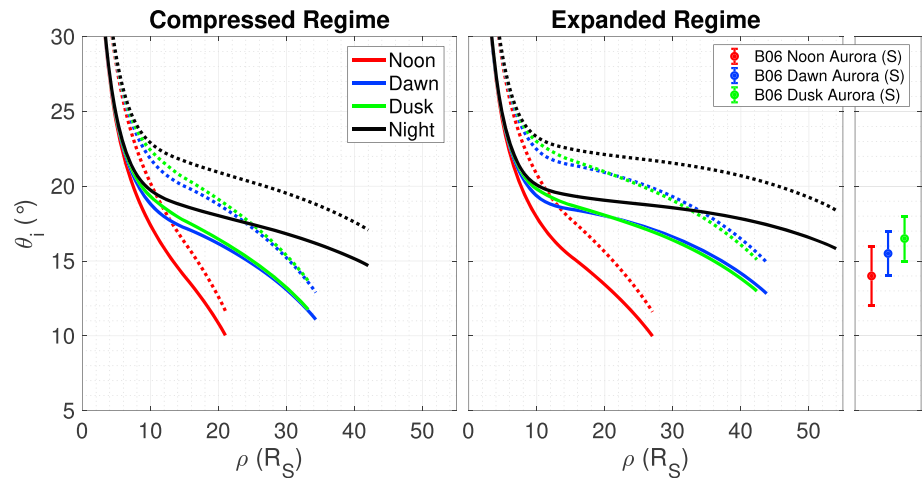


Figure 6. Profiles showing the mapping of magnetic field lines from the equatorial plane to the northern (solid lines) and southern (dotted lines) polar ionospheres, with local time sector shown by the color. Ionospheric colatitude θ_i is measured relative to the northern pole for northern hemisphere values and the southern pole for southern hemisphere values. Also shown by the solid circles with error bars are median locations and widths of the main auroral oval in the southern hemisphere for different local time sectors as shown by the color, from a statistical study by Badman et al. (2006). Model values shown here are provided in tables in the supporting information.

model calculations have been used in Sergis et al. (2018) to confirm that hot plasma pressure is approximately uniform along magnetic field lines, using high-latitude proximal Cassini orbits.

The resulting values are shown in Figure 6, with northern hemisphere values shown by solid lines and southern hemisphere counterparts shown by dotted lines. All values shown in Figure 6 are also provided in tables in the supporting information. Also shown by the colored solid circles with error bars are the average locations and widths of the main auroral oval for noon, dawn, and dusk local time sectors, respectively, estimated from a statistical study of multiple Hubble Space Telescope observations of the ultraviolet aurora in the southern hemisphere from Badman et al. (2006). As these observations were of the southern hemisphere only, they should be compared with the dotted lines of the model outputs.

It can clearly be seen that there is significant variation in ionospheric mapping of field lines for different local time sectors. In particular, the locations of the open-closed field line boundary (OCFLB), shown by the colatitude of the most radially distant point for each profile, vary greatly between sectors. We can see that the OCFLB maps to more polar regions in the noon sector, with $\sim 10^\circ$ (11.5°) for the northern (southern) hemisphere, than for the night sector, with $\sim 15.5^\circ$ (17.5°) for the northern (southern) hemisphere. This behavior is qualitatively in agreement with the results of Carbary (2018), who find corresponding values of $\sim 13^\circ$ (16°) for the dayside and $\sim 16^\circ$ (18°) for the nightside, using a data-based magnetic field model. Our noon sector values are somewhat lower than the dayside values of Carbary (2018); however, if we were to consider some combination of our noon, dawn, and dusk values to represent the entire dayside hemisphere, for a more appropriate comparison, they would likely be in better agreement. This is because the values for dawn and dusk are both higher than the noon value alone.

In addition, for the compressed regime in particular, we find a slight dawn-dusk asymmetry in the location of the OCFLB, with the dusk location around 1° equatorward of the dawn location. It can be seen on close inspection of Figure 6 that this asymmetry is mainly due to the small asymmetry in magnetopause radius in these models, rather than the influence of the hot plasma pressure profiles on the magnetic field structure. This is evident as the two profiles are broadly coincident in the outer magnetosphere until the dusk model terminates at $\rho = 33.2 R_S$, in comparison to dawn's $34.3 R_S$ (see Table 2). It is interesting to note that this relationship is qualitatively similar to that observed by Badman et al. (2006), who found that on average the main auroral oval in the dusk sector was located $\sim 1^\circ$ equatorward of the aurora in the dawn sector, in the southern hemisphere. Furthermore, the dawn aurora was observed to be $\sim 1.5^\circ$ equatorward of the noon auroral location in Badman et al. (2006). This is approximately the same as the difference in the OCFLB we observe between our noon and dawn models for the compressed regime, southern hemisphere values, as shown in the first panel of Figure 6 (although the difference is significantly higher for the expanded regime).

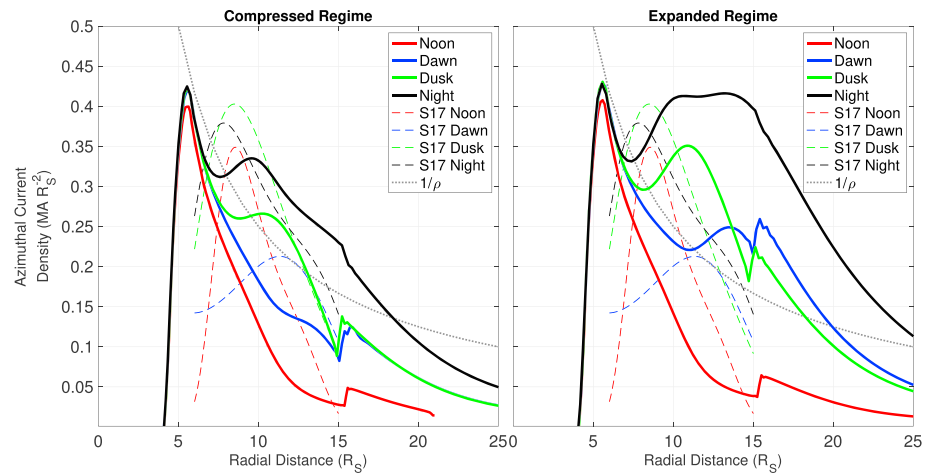


Figure 7. Solid lines show profiles of equatorial azimuthal current density with radial distance, for each local time sector model as shown by the color, for compressed (left) and expanded (right) regimes. Dashed lines in each color show corresponding profiles from Sergis et al. (2017) estimated in the radial range $6 - 15R_S$ using Cassini observations (left and right plots an exact reproduction). The gray dotted line shows a representative profile with current density inversely proportional to radial distance, as for a Connerney et al., (1981, 1983) style ring current model.

Such a comparison supports the hypothesis from this and other studies, that the main auroral oval may map to regions in the outer equatorial magnetosphere, within a few R_S of the OCFLB. In addition, a later study by Badman et al. (2011) of Saturn's infrared aurora found that the nightside main oval was persistently $\sim 2^\circ$ equatorward of the dayside, in line with the aforementioned day-night asymmetry we observe in our OCFLB. It is interesting to note that this agreement is achieved despite the shielding field associated with the UCL/AGA model, discussed in Section 2.4, being a less accurate approximation in the higher latitude regions, beyond around 50° latitude (Caudal, 1986).

Now comparing the results for the compressed and expanded regimes, we see that the differences between the profiles are not as extreme as the differences between local time sectors. This suggests that variations in external solar wind conditions do not have a significant impact on the magnetic mapping between ionosphere and the equatorial disk. In particular for the noon sector, the profiles for the compressed and expanded regimes are very similar, with near coincident locations of the OCFLB, and similar regions of the equatorial magnetosphere mapping to similar values of θ_i in each case. For example, the equatorial radial distance corresponding to the outer one-third of the noon sector magnetosphere for each regime, maps to roughly the same θ_i for each case, $\sim 14^\circ$ in the north, and $\sim 16.5^\circ$ in the south. A similar result was found in Bunce et al. (2008), who used an adapted "CAN"-type (Connerney et al., 1981, 1983) ring current model from Bunce et al. (2007) to investigate how ionospheric mapping varied with system size in the noon sector magnetosphere. They found only a very modest variation with system size, for a noon magnetopause radius range of $16 - 26R_S$, comparable to the range in this work. Bunce et al. (2008) then used the results of this modeling, in combination with Hubble Space Telescope observations of the ultraviolet aurora and Cassini data, to show that the noon aurora are indeed likely to lie near the boundary between open and closed magnetic field lines. These authors go on to suggest that the quasi-continuous main auroral oval corresponds to the OCFLB at other local time sectors, in line with our interpretation here. Combining results for all local time sectors and compressed/expanded regimes, we find a mean location of the OCFLB equal to 12.4° in the north and 14.4° in the south. This is comparable to recent results from a Cassini multi-instrument study from Jinks et al. (2014), who find corresponding values of 13.3° in the north and 15.6° . In that study, the majority of observations are from the post-midnight sector where we expect the OCFLB to be more equatorward, which may explain why their average values are a little higher than ours.

When interpreting ionospheric-equatorial magnetic mappings, it is also pertinent to consider how the total current density varies with radial distance in the equatorial magnetosphere. Predictions for total azimuthal current density at the equator for each local time sector model, for compressed and expanded regimes, are shown in Figure 7. (Note that as the magnetodisk model is azimuthally axisymmetric, and hence used here to represent individual local time sectors separately, radial currents are not directly predicted.) Superimposed on each plot is a representative profile with azimuthal current density inversely proportional to cylindrical

radial distance ρ , as is the case for CAN-type ring current model constructions from Connerney et al. (1981, 1983).

We can clearly see significant dawn-dusk and noon-night asymmetry in the model current density profiles, with higher magnitudes for the dusk and night sector models, for both the compressed and expanded regimes. This is due to the similar relationship between the different input equatorial hot plasma pressure profiles for each local time sector, shown in Figure 1, enhancing the component of the ring current associated with the hot plasma pressure gradient. In addition, the underlying magnetic field structure, and the centrifugal force on the cold plasma, both influence the current density profile via equation (1). This helps explain the significant difference in all profiles between the compressed and expanded regimes, with larger models having in general higher magnitude predicted azimuthal currents, due to lower magnetic field strengths at the equator as shown in Figure 2. The nightside models in particular have much higher predicted current densities than all other sector models for this reason. Similar results were also shown in a study by Jia et al. (2012); in that study, the authors presented results of MHD simulations of Saturn's magnetosphere and ionosphere and found that the predicted azimuthal current density had a persistent local time asymmetry, being higher by a factor of ~ 2 across the nightside than at other local times, with predicted broad peak of ~ 100 pA/m² (0.36 MA/ R_S^2) on the nightside at around 10 – 15 R_S radial distance. Through comparison with the dashed lines on Figure 7, we can see that our observed local time asymmetry is also broadly in agreement with the results of Sergis et al. (2017), who used long-term averages of properties measured from Cassini MAG, MIMI, and CAPS observations to make estimates of the typical distribution of equatorial azimuthal current density at local time sectors. Due to the complexity and the strong temporal variability of the system, Sergis et al. (2017) estimate the uncertainty in their presented current values as $\sim 50\%$, which is not shown on the plot but must be considered when directly comparing these results with our model predictions. It can be seen that Sergis et al. (2017) found the peak and overall current densities were higher for the dusk and midnight sectors than the dawn and noon sectors, though with peaks closer in to the planet than the Jia et al. (2012) results, at around the 7 – 13 R_S radial range. This observed variation in peak location between our model results and those of Sergis et al. (2017) and Jia et al. (2012) is likely associated with the variation in approaches used to model both the hot and cold plasma pressure populations, as the calculated currents are sensitive to the exact parameterizations. It is interesting to note that for our expanded regime models, the region $\rho \approx 13$ R_S where the current density at dawn surpasses the current density at dusk is approximately coincident with the region where the dawn magnetic field structure becomes more disk-like than dusk, as shown by the crossing of the blue and green lines in Figure 5 right panel. This further illustrates the relationship between ring current intensity and magnetodisk magnetic field structure.

Our overall results considered across all local times are also broadly consistent with the observation-based estimates from Kellett et al. (2011) and Carbary et al. (2012). Kellett et al. (2011) analyzed Cassini magnetic field and plasma data from 11 near-equatorial orbits and observed a rapid increase in current density from around 5 R_S to a peak of around 90 pA/m² (~ 0.33 MA/ R_S^2) at ~ 9 R_S radial distance, before falling more gradually to below 20 pA/m² (0.07 MA/ R_S^2) at ~ 20 R_S . Kellett et al. (2011) found only modest local time asymmetry in current density, perhaps in part due to limited observations across different sectors for this early study. Carbary et al. (2012) used magnetic field data from the first 5 years of the Cassini mission binned without accounting for local time and similarly found a sharp rise in calculated azimuthal current density to a peak of around 75 pA/m² (0.27 MA/ R_S^2) at ~ 9.5 R_S radial distance, before a more gradual drop off. In that study, the estimated current sheet profile was also compared directly to predictions from the earlier UCL/AGA model of Achilleos et al. (2010), and the two profiles showed considerable agreement. Only our expanded nightside model shows peak and overall current density predictions that are perhaps unrealistically high in magnitude when compared to results of previous studies; this may be due to a particularly low equatorial magnetic field strength magnitude predicted for this model as shown in Figure 2, requiring an intense azimuthal current to maintain force balance in the magnetosphere. This low field strength is in turn caused by the choice of a perhaps artificially large magnetopause radius of $R_D = 54$ R_S for this expanded nightside model, as discussed previously in section 3.1 in the context of Figure 3.

From Figure 7 we can also see that for all local time sectors, beyond the local maximum region, the equatorial current density falls more quickly than the $1/\rho$ decrease predicted by a CAN-type ring current model. Similar behavior is also clearly shown was also found in the results from the observational study from Sergis et al. (2017). This suggests that the more complex ring current structure enabled by the modified UCL/AGA model used in this study may be more appropriate at characterizing the true structure of Saturn's equatorial current

sheet than a CAN-type model. However, both types of model give similar predictions for the magnetic field away from the edges of the CAN disk, as discussed in Achilleos et al. (2010). Furthermore, in Achilleos et al. (2010), the UCL/AGA model predictions of azimuthal current density were validated by comparing to data-derived currents from Sergis et al. (2010).

4. Summary and Conclusions

In this study we have used the 2-D, force-balance UCL/AGA model from Achilleos et al. (2010) to describe the typical, equilibrium conditions of Saturn's magnetosphere at four different local time sectors. We have used equatorial profiles of hot plasma pressure at different local times from Sergis et al. (2017), and a magnetopause surface model from Pilkington et al. (2015b), to investigate how global hot plasma content and system size influence the magnetospheric structure at different local times.

We have found that, as expected, there is significant day-night asymmetry in the magnetic field structure of the magnetosphere and that this is mainly due to the large asymmetry in magnetopause radius between day and night. We also find a small dawn-dusk asymmetry in the magnetic field structure, with both the hot plasma content and magnetopause radius having comparable influence. For the compressed regime, where the magnetosphere is under high solar wind dynamic pressure conditions, we find that the dusk sector magnetic field is more disk-like due to the influence of the increased hot plasma pressure in that sector. Meanwhile, for the expanded regime we find the opposite is true and that the dawn magnetic field is more disk-like, due to the larger magnetopause radius at dawn for this regime. Importantly, we also find significant differences in how equatorial magnetic field lines map to the polar ionosphere for the different local time sector models, with field lines from the outer magnetosphere mapping to far more equatorward regions of the ionosphere on the nightside than the dayside. This result is useful in particular when interpreting auroral observations at Saturn's ionosphere and attempting to ascertain their origins in the magnetosphere. These results may also be useful for future studies looking at local time variations in other magnetospheric properties, such as current sheet thickness.

The simplicity of the modeling approach used in this work means that many magnetospheric properties can be easily compared between different local time sectors. However, a consequence of this is that any dynamical behavior, such as reconnection events or plasmoids, cannot be directly captured. In addition, due to the assumed axisymmetry of each model, we cannot investigate the influence of any observed local time asymmetry in azimuthal phenomena. For example, a nonnegligible dawn-dusk asymmetry in the azimuthal bend-back of magnetic field lines in the direction opposite to planetary rotation has been observed, with more substantial bend-back in the dawn sector than the dusk sector (e.g., Delamere et al., 2015). This may affect our assumptions of how magnetospheric plasma properties vary with radial distance, such as the angular velocity, which in turn influences our estimates of centrifugal force. In Jia and Kivelson (2016), the authors offer a formulation for how the force-balance assumption of equation (1) could be modified to account for a local time variation in radial outflow of plasma. While a preliminary investigation suggests this approach would not have a significant impact on our results, it would be worthwhile to investigate this further in a future study.

In summary, this study shows that there is a significant local time variation in the magnetic field structure of Saturn's magnetosphere. The equatorial current sheet thickness, current density, and magnetic mapping to the ionosphere all vary depending on both local time and external solar wind pressure conditions, due to force balance within the magnetosphere in this study. Our results are useful for potential future studies looking to interpret a range of phenomena at Saturn, from reconnection events and plasmoids to auroral oval modulations.

References

- Achilleos, N., Arridge, C. S., Bertucci, C., Guio, P., Romanelli, N., & Sergis, N. (2014). A combined model of pressure variations in Titan's plasma environment. *Geophysical Research Letters*, *41*, 8730–8735. <https://doi.org/10.1002/2014GL061747>
- Achilleos, N., Arridge, C., Bertucci, C., Jackman, C., Dougherty, M., Khurana, K., & Russell, C. (2008). Large-scale dynamics of Saturn's magnetopause: Observations by Cassini. *Journal of Geophysical Research*, *113*, A11209. <https://doi.org/10.1029/2008JA013265>
- Achilleos, N., Guio, P., & Arridge, C. S. (2010). A model of force balance in Saturn's magnetodisc. *Monthly Notices of the Royal Astronomical Society*, *401*(4), 2349–2371. <https://doi.org/10.1111/j.1365-2966.2009.15865.x>
- Achilleos, N., Guio, P., Arridge, C. S., Sergis, N., Wilson, R., Thomsen, M., & Coates, A. J. (2010). Influence of hot plasma pressure on the global structure of Saturn's magnetodisk. *Geophysical Research Letters*, *37*, L20201. <https://doi.org/10.1029/2010GL045159>

Acknowledgments

All relevant Cassini data can be accessed via the Planetary Data System (<http://pds.nasa.gov/>). A. M. S. thanks J. Carbary for providing the magnetic field traces shown in Figure 3. A. M. S. was supported by the UK Science and Technology Facilities Council (STFC) through a PhD studentship (UCL Astrophysics, ST/N50449X/1). N. A. and P. G. were supported by the UK STFC Consolidated Grant (UCL/MSSL Solar and Planetary Physics, ST/N000722/1). C. S. A. was supported by a Royal Society Research Fellowship. N. S. was supported by Subcontract No. 110511 between JHU/JPL and the Academy of Athens.

- Alexeev, I., & Belenkaya, E. (2005). Modeling of the Jovian magnetosphere. *Annales Geophysicae*, 23(3), 809–826. <https://doi.org/10.5194/angeo-23-809-2005>
- Alexeev, I. I., Kalegaev, V. V., Belenkaya, E. S., Bobrovnikov, S. Y., Bunce, E. J., Cowley, S. W. H., & Nichols, J. D. (2006). A global magnetic model of Saturn's magnetosphere and a comparison with Cassini SOI data. *Geophysical Research Letters*, 33, L08101. <https://doi.org/10.1029/2006GL025896>
- Arridge, C., Achilleos, N., Dougherty, M., Khurana, K., & Russell, C. (2006). Modeling the size and shape of Saturn's magnetopause with variable dynamic pressure. *Journal of Geophysical Research*, 111, A11227. <https://doi.org/10.1029/2005JA011574>
- Arridge, C. S., McAndrews, H. J., Jackman, C. M., Forsyth, C., Walsh, A. P., Sittler, E. C., & Young, D. T. (2009). Plasma electrons in Saturn's magnetotail: Structure, distribution and energisation. *Planetary and Space Science*, 57, 2032–2047. <https://doi.org/10.1016/j.pss.2009.09.007>
- Arridge, C., Russell, C., Khurana, K., Achilleos, N., Cowley, S., Dougherty, M., & Bunce, E. (2008). Saturn's magnetodisc current sheet. *Journal of Geophysical Research*, 113, A04214. <https://doi.org/10.1029/2007JA012540>
- Badman, S. V., Achilleos, N., Baines, K. H., Brown, R. H., Bunce, E. J., Dougherty, M. K., & Stallard, T. (2011). Location of Saturn's northern infrared aurora determined from Cassini VIMS images. *Geophysical Research Letters*, 38, L03102. <https://doi.org/10.1029/2010GL046193>
- Badman, S. V., Cowley, S. W. H., Gérard, J. C., & Grodent, D. (2006). A statistical analysis of the location and width of Saturn's southern auroras. *Annales Geophysicae*, 24, 3533–3545. <https://doi.org/10.5194/angeo-24-3533-2006>
- Bunce, E. J., Arridge, C. S., Clarke, J. T., Coates, A. J., Cowley, S. W. H., Dougherty, M. K., & Talboys, D. L. (2008). Origin of Saturn's aurora: Simultaneous observations by Cassini and the Hubble Space Telescope. *Journal of Geophysical Research*, 113, A09209. <https://doi.org/10.1029/2008JA013257>
- Bunce, E. J., Arridge, C. S., Cowley, S. W. H., & Dougherty, M. K. (2008). Magnetic field structure of Saturn's dayside magnetosphere and its mapping to the ionosphere: Results from ring current modeling. *Journal of Geophysical Research*, 113, A02207. <https://doi.org/10.1029/2007JA012538>
- Bunce, E., Cowley, S., Alexeev, I., Arridge, C., Dougherty, M., Nichols, J., & Russell, C. (2007). Cassini observations of the variation of Saturn's ring current parameters with system size. *Journal of Geophysical Research*, 112, A10202. <https://doi.org/10.1029/2007JA012275>
- Carbary, J. F. (2018). The meridional magnetic field lines of Saturn. *Journal of Geophysical Research: Space Physics*, 123, 6264–6276. <https://doi.org/10.1029/2018JA025628>
- Carbary, J., Achilleos, N., & Arridge, C. (2012). Statistical ring current of Saturn. *Journal of Geophysical Research*, 117, A06223. <https://doi.org/10.1029/2011JA017472>
- Caudal, G. (1986). A self-consistent model of Jupiter's magnetodisc including the effects of centrifugal force and pressure. *Journal of Geophysical Research*, 91(A4), 4201–4221.
- Clarke, K. E., Andrews, D. J., Arridge, C. S., Coates, A. J., & Cowley, S. W. H. (2010). Magnetopause oscillations near the planetary period at Saturn: Occurrence, phase, and amplitude. *Journal of Geophysical Research*, 115, A08209. <https://doi.org/10.1029/2009JA014745>
- Connerney, J. E. P., Acuna, M. H., & Ness, N. F. (1981). Saturn's ring current and inner magnetosphere. *Nature*, 292, 724–726. <https://doi.org/10.1038/292724a0>
- Connerney, J. E. P., Acuna, M. H., & Ness, N. F. (1983). Currents in Saturn's magnetosphere. *Journal of Geophysical Research*, 88, 8779–8789. <https://doi.org/10.1029/JA088iA11p08779>
- Cowley, S. W. H., & Provan, G. (2017). Planetary period modulations of Saturn's magnetotail current sheet during northern spring: Observations and modeling. *Journal of Geophysical Research: Space Physics*, 122, 6049–6077. <https://doi.org/10.1002/2017JA023993>
- Delamere, P. A., Otto, A., Ma, X., Bagenal, F., & Wilson, R. J. (2015). Magnetic flux circulation in the rotationally driven giant magnetospheres. *Journal of Geophysical Research: Space Physics*, 120, 4229–4245. <https://doi.org/10.1002/2015JA021036>
- Desch, M. D., & Kaiser, M. L. (1981). Voyager measurement of the rotation period of Saturn's magnetic field. *Geophysical Research Letters*, 8, 253–256. <https://doi.org/10.1029/GL008i003p00253>
- Dougherty, M. K., Cao, H., Khurana, K. K., Hunt, G. J., Provan, G., Kellock, S., & Southwood, D. J. (2018). Saturn's magnetic field revealed by the Cassini Grand Finale. *Science*, 362, 6410. <https://doi.org/10.1126/science.aat5434>
- Dougherty, M. K., Kellock, S., Southwood, D. J., Balogh, A., Smith, E. J., Tsurutani, B. T., & Cowley, S. W. H. (2004). The Cassini magnetic field investigation. *Space Science Reviews*, 114, 331–383. <https://doi.org/10.1007/s11214-004-1432-2>
- Dougherty, M., Khurana, K., Neubauer, F., Russell, C., Saur, J., Leisner, J., & Burton, M. (2006). Identification of a dynamic atmosphere at Enceladus with the Cassini magnetometer. *Science*, 311(5766), 1406–1409. <https://doi.org/10.1126/science.1120985>
- Espinosa, S., & Dougherty, M. (2001). Unexpected periodic perturbations in Saturn's magnetic field data from Pioneer 11 and Voyager 2. *Advances in Space Research*, 28(6), 919–924.
- Espinosa, S. A., Southwood, D. J., & Dougherty, M. K. (2003). Reanalysis of Saturn's magnetospheric field data view of spin-periodic perturbations. *Journal of Geophysical Research*, 108, 1085. <https://doi.org/10.1029/2001JA005083>
- Gérard, J. C., Bonfond, B., Gustin, J., Grodent, D., Clarke, J. T., Bisikalo, D., & Shematovich, V. (2009). Altitude of Saturn's aurora and its implications for the characteristic energy of precipitated electrons. *Geophysical Research Letters*, 36, L02202. <https://doi.org/10.1029/2008GL036554>
- Hunt, G. J., Cowley, S. W. H., Provan, G., Bunce, E. J., Alexeev, I. I., Belenkaya, E. S., & Coates, A. J. (2014). Field-aligned currents in Saturn's southern nightside magnetosphere: Subcorotation and planetary period oscillation components. *Journal of Geophysical Research: Space Physics*, 119, 9847–9899. <https://doi.org/10.1002/2014JA020506>
- Jia, X., Hansen, K. C., Gombosi, T. I., Kivelson, M. G., Tóth, G., DeZeeuw, D. L., & Ridley, A. J. (2012). Magnetospheric configuration and dynamics of Saturn's magnetosphere: A global MHD simulation. *Journal of Geophysical Research*, 117, A05225. <https://doi.org/10.1029/2012JA017575>
- Jia, X., & Kivelson, M. G. (2016). Dawn-dusk asymmetries in rotating magnetospheres: Lessons from modeling Saturn. *Journal of Geophysical Research: Space Physics*, 121, 1413–1424. <https://doi.org/10.1002/2015JA021950>
- Jia, X., Kivelson, M. G., & Gombosi, T. I. (2012). Driving Saturn's magnetospheric periodicities from the upper atmosphere/ionosphere. *Journal of Geophysical Research*, 117, A04215. <https://doi.org/10.1029/2011JA017367>
- Jinks, S. L., Bunce, E. J., Cowley, S. W. H., Provan, G., Yeoman, T. K., Arridge, C. S., & Wahlund, J. E. (2014). Cassini multi-instrument assessment of Saturn's polar cap boundary. *Journal of Geophysical Research: Space Physics*, 119, 8161–8177. <https://doi.org/10.1002/2014JA020367>
- Kanani, S., Arridge, C. S., Jones, G., Fazakerley, A., McAndrews, H., Sergis, N., et al. (2010). A new form of Saturn's magnetopause using a dynamic pressure balance model, based on in situ, multi-instrument Cassini measurements. *Journal of Geophysical Research*, 115, A06207. <https://doi.org/10.1029/2009JA014262>
- Kellett, S., Arridge, C. S., Bunce, E. J., Coates, A. J., Cowley, S. W. H., Dougherty, M. K., & Wilson, R. J. (2011). Saturn's ring current: Local time dependence and temporal variability. *Journal of Geophysical Research*, 116, A05220. <https://doi.org/10.1029/2010JA016216>

- Khurana, K. K., Kivelson, M. G., Vasyliunas, V. M., Krupp, N., Woch, J., Lagg, A., & Kurth, W. S. (2004). The configuration of Jupiter's magnetosphere. *Jupiter. The Planet, Satellites and Magnetosphere*, 1, 593–616.
- Kivelson, M. G., & Jia, X. (2014). Control of periodic variations in Saturn's magnetosphere by compressional waves. *Journal of Geophysical Research: Space Physics*, 119, 8030–8045. <https://doi.org/10.1002/2014JA020258>
- Krimigis, S. M., Mitchell, D. G., Hamilton, D. C., Livi, S., Dandouras, J., Jaskulek, S., & Williams, D. J. (2004). Magnetosphere Imaging Instrument (MIMI) on the Cassini mission to Saturn/Titan. *Space Science Reviews*, 114, 233–329. <https://doi.org/10.1007/s11214-004-1410-8>
- McAndrews, H. J., Thomsen, M. F., Arridge, C. S., Jackman, C. M., Wilson, R. J., Henderson, M. G., & Dougherty, M. K. (2009). Plasma in Saturn's nightside magnetosphere and the implications for global circulation. *Planetary and Space Science*, 57, 1714–1722. <https://doi.org/10.1016/j.pss.2009.03.003>
- Petrinec, S., & Russell, C. (1997). Hydrodynamic and MHD equations across the bow shock and along the surfaces of planetary obstacles. *Space Science Reviews*, 79(3-4), 757–791.
- Pilkington, N. M., Achilleos, N., Arridge, C. S., Guio, P., Masters, A., Ray, L., & Dougherty, M. (2015a). Internally driven large-scale changes in the size of Saturn's magnetosphere. *Journal of Geophysical Research: Atmospheres*, 120, 7289–7306. <https://doi.org/10.1002/2015JA021290>
- Pilkington, N. M., Achilleos, N., Arridge, C. S., Guio, P., Masters, A., Ray, L. C., & Dougherty, M. K. (2015b). Asymmetries observed in Saturn's magnetopause geometry. *Geophysical Research Letters*, 42, 6890–6898. <https://doi.org/10.1002/2015GL065477>
- Ramer, K. M., Kivelson, M. G., Sergis, N., Khurana, K. K., & Jia, X. (2017). Spinning, breathing, and flapping: Periodicities in Saturn's middle magnetosphere. *Journal of Geophysical Research: Space Physics*, 122, 393–416. <https://doi.org/10.1002/2016JA023126>
- Seidemann, P. K., Archinal, B. A., A'Hearn, M. F., Conrad, A., Consolmagno, G. J., Hestroffer, D., & Williams, I. P. (2007). Report of the IAU/IAG Working Group on cartographic coordinates and rotational elements: 2006. *Celestial Mechanics and Dynamical Astronomy*, 98, 155–180. <https://doi.org/10.1007/s10569-007-9072-y>
- Sergis, N., Achilleos, N., Guio, P., Arridge, C., Sorba, A., Roussos, E., et al. (2018). Mapping Saturn's night side plasma sheet using Cassini's proximal orbits. *Geophysical Research Letters*, 45, 6798–6804. <https://doi.org/10.1029/2018GL078141>
- Sergis, N., Arridge, C. S., Krimigis, S. M., Mitchell, D. G., Rymer, A. M., Hamilton, D. C., & Coates, A. J. (2011). Dynamics and seasonal variations in Saturn's magnetospheric plasma sheet, as measured by Cassini. *Journal of Geophysical Research*, 116, A04203. <https://doi.org/10.1029/2010JA016180>
- Sergis, N., Jackman, C. M., Thomsen, M. F., Krimigis, S. M., Mitchell, D. G., Hamilton, D. C., & Wilson, R. J. (2017). Radial and local time structure of the Saturnian ring current, revealed by Cassini. *Journal of Geophysical Research: Space Physics*, 122, 1803–1815. <https://doi.org/10.1002/2016JA023742>
- Sergis, N., Krimigis, S., Mitchell, D., Hamilton, D., Krupp, N., Mauk, B., & Dougherty, M. (2007). Ring current at Saturn: Energetic particle pressure in Saturn's equatorial magnetosphere measured with Cassini/MIMI. *Geophysical Research Letters*, 34, L09102. <https://doi.org/10.1029/2006GL029223>
- Sergis, N., Krimigis, S., Roelof, E., Arridge, C. S., Rymer, A., Mitchell, D., et al. (2010). Particle pressure, inertial force, and ring current density profiles in the magnetosphere of Saturn, based on Cassini measurements. *Geophysical Research Letters*, 37, L02102. <https://doi.org/10.1029/2009GL041920>
- Shue, J. H., Chao, J., Fu, H., Russell, C., Song, P., Khurana, K., & Singer, H. (1997). A new functional form to study the solar wind control of the magnetopause size and shape. *Journal of Geophysical Research*, 102(A5), 9497–9511.
- Sorba, A. M., Achilleos, N. A., Guio, P., Arridge, C. S., Pilkington, N. M., Masters, A., & Dougherty, M. K. (2017). Modeling the compressibility of Saturn's magnetosphere in response to internal and external influences. *Journal of Geophysical Research: Space Physics*, 122, 1572–1589. <https://doi.org/10.1002/2016JA023544>
- Sorba, A. M., Achilleos, N. A., Guio, P., Arridge, C. S., Sergis, N., & Dougherty, M. K. (2018). The periodic flapping and breathing of Saturn's magnetodisk during equinox. *Journal of Geophysical Research: Space Physics*, 123, 8292–8316. <https://doi.org/10.1029/2018JA025764>
- Spreiter, J. R., Alksne, A. Y., & Abraham-Shrauner, B. (1966). Theoretical proton velocity distributions in the flow around the magnetosphere. *Planetary and Space Science*, 14, 1207–1220. [https://doi.org/10.1016/0032-0633\(66\)90033-X](https://doi.org/10.1016/0032-0633(66)90033-X)
- Stallard, T. S., Melin, H., Miller, S., Badman, S. V., Brown, R. H., & Baines, K. H. (2012). Peak emission altitude of Saturn's H₃⁺ aurora. *Geophysical Research Letters*, 39, L15103. <https://doi.org/10.1029/2012GL052806>
- Stern, D. P. (1970). Euler Potentials. *American Journal of Physics*, 38, 494–501. <https://doi.org/10.1119/1.1976373>
- Thomsen, M. F., Jackman, C. M., Cowley, S. W. H., Jia, X., Kivelson, M. G., & Provan, G. (2017). Evidence for periodic variations in the thickness of Saturn's nightside plasma sheet. *Journal of Geophysical Research: Space Physics*, 122, 280–292. <https://doi.org/10.1002/2016JA023368>
- Wilson, R. J., Bagenal, F., & Persoon, A. M. (2017). Survey of thermal plasma ions in Saturn's magnetosphere utilizing a forward model. *Journal of Geophysical Research: Space Physics*, 122, 7256–7278. <https://doi.org/10.1002/2017JA024117>
- Wilson, R., Tokar, R., Henderson, M., Hill, T., Thomsen, M., & Pontius, D. (2008). Cassini plasma spectrometer thermal ion measurements in Saturn's inner magnetosphere. *Journal of Geophysical Research*, 113, A12218. <https://doi.org/10.1029/2008JA013486>
- Young, D. T., Berthelier, J. J., Blanc, M., Burch, J. L., Coates, A. J., Goldstein, R., & Zinsmeyer, C. (2004). Cassini plasma spectrometer investigation. *Space Science Reviews*, 114, 1–112. <https://doi.org/10.1007/s11214-004-1406-4>